Quantum control of coupled two-electron dynamics in quantum dots

Quantum control of coupled two-electron dynamics in quantum dots

R Nepstad[1], L Sælen[1,2], I Degani[3] and J P Hansen[1]

[1] Department of Physics and Technology, University of Bergen, N-5007 Bergen, Norway
[2] Laboratoire de Chimie Physique-Matière et Rayonnement, Université Pierre et Marie Curie—CNRS, F-75005 Paris, France
[3] Department of Mathematics, University of Bergen, N-5008 Bergen, Norway

Abstract
We investigate optimal control strategies for state to state transitions in a model of a quantum dot molecule containing two active strongly interacting electrons. The Schrödinger equation is solved nonperturbatively in conjunction with several quantum control strategies. This results in optimized electric pulses in the terahertz regime which can populate combinations of states with very short transition times. The speed-up compared to intuitively constructed pulses is an order of magnitude. We furthermore make use of optimized pulse control in the simulation of an experimental preparation of the molecular quantum dot system. It is shown that exclusive population of certain excited states leads to a complete suppression of spin dephasing, as was indicated in Nepstad *et al* (2008 *Phys. Rev.* B **77** 125315).

(Some figures in this article are in colour only in the electronic version)

1. Introduction

Application of quantum control theory to optimize transitions in strongly interacting quantum systems is a well-established technology in simple two-level systems [1]. In more complex or open systems involving many important channels it is in general much more complicated to improve the probability of the desired reactions and transitions. This is true in systems as diverse as dipole blockade dynamics in cold Rydberg gases [2] and electron dynamics in semiconductor two-electron quantum dot systems [3]. In the latter, which is our case, the electron–electron interaction is comparable to other interactions in the system and cannot be neglected. The ability to achieve fast and optimized transitions in such systems, and a variety of others, is important for improving present-day technology in quantum information, metrology and quantum chemistry.

In few-electron quantum dots it is well recognized that interactions with the substrate will induce decoherence, which limits the ability to utilize unique quantum properties such as entanglement. Examples of such interactions are hyperfine and spin–orbit interactions between the quantum dot electrons and surrounding atoms, and interactions with phonons in the substrate lattice. As strategies to reduce decoherence, one can either carry out experiments in systems and at temperatures which minimize unwanted interactions, or try to develop

methods to perform the required transitions much faster than the characteristic timescale of the decoherence. We have previously demonstrated that intuitively selected microwave pulses can populate both single states and more complex states of the lowest excitation bands and we were able to further decrease the transition time in the first case by optimal pulse control [3].

In the present work we optimize time-dependent transitions to more complex target states and compare various strategies of optimization including frequency-selective control algorithms [4]. We show that more advanced control strategies lead to a factor of seven faster transition times than previously reported using intuitively constructed pulses. In the second part we address the application of quantum control inside regions of anticrossings. This is related to recent experiments [5, 6] which measure spin dephasing of the system through hyperfine interactions with the surrounding nuclear spin bath. The experiment was simulated in Nepstad *et al* [7] and very good agreement between theory and experiment was achieved. In the same work, we further demonstrated how populating higher excited states could be used as a method to inhibit decoherence. In this paper we apply the technique of optimal control theory to exclusively populate such states during initial set-up of the experiment. Section 2 describes the theory in detail. In section 3 we present the results, followed by concluding remarks.

2. Theory and methods

In this section we review and detail the numerical methods used to study dynamics of a two-dimensional, two-electron double dot exposed to electric and magnetic fields. This includes DC and pulsed electric fields and weak, locally varying magnetic fields representing the hyperfine interaction [3, 7, 8].

2.1. Model

The two-dimensional single-particle effective mass Hamiltonian of our system is

$$h_0(x, y) = -\frac{\hbar^2}{2m^*}\nabla^2 + \frac{1}{2}m^*\omega^2\left[\left(|x| - \frac{d}{2}\right)^2 + y^2\right]. \quad (1)$$

Combined with the electron–electron interaction term, the total field-free Hamiltonian becomes

$$H_0 = h_0(\mathbf{r}_1) + h_0(\mathbf{r}_2) + \frac{e^2}{4\pi\epsilon_r\epsilon_0 r_{12}}. \quad (2)$$

Here $\mathbf{r}_{1,2}$ are single-particle coordinates. The material parameters may take on different values to reflect various physical systems. In this paper we will use values compatible with GaAs quantum dots, where $m^* = 0.067m_e$ (effective mass), $\epsilon_r = 12.4$ (relative permittivity). The electron mass is denoted m_e. The confinement strength is set to $\hbar\omega = 1$ meV and the interdot separation to $d = 130$ nm, which are realistic experimental values [9, 10]. In subsequent sections we will introduce time-dependent terms, including interaction with external electromagnetic fields and the spin bath of the embedding substrate.

The eigenstates of the field-free Hamiltonian H_0 are expanded in properly symmetrized products of Hermite functions. The Hermite functions are the familiar solutions of the single-particle harmonic oscillator in two dimensions, which are $\phi(x, y) = \mathcal{N}e^{-m^*\omega(x^2+y^2)/2}H_{n_x}(x\sqrt{m^*\omega})H_{n_y}(y\sqrt{m^*\omega})$, where H_n is a Hermite polynomial. The symmetrized expansion now is $\Psi = \sum_{j\geqslant i}^{n_{max}} c_{ij}|ij\rangle$, where

$$|ij\rangle = \begin{cases} \frac{1}{\sqrt{2}}[\phi_i(\mathbf{r}_1)\phi_j(\mathbf{r}_2) \pm \phi_j(\mathbf{r}_1)\phi_i(\mathbf{r}_2)] & i \neq j \\ \phi_i(\mathbf{r}_1)\phi_j(\mathbf{r}_2) & i = j, \end{cases} \quad (3)$$

and $i = \{n_x, n_y\}$, $j = \{n'_x, n'_y\}$ represent different sets of quantum numbers. The symmetric and antisymmetric basis functions correspond to singlet and triplet states, respectively. This basis has the advantage of yielding analytic expressions for the matrix elements of each term in equation (2). A detailed exposition of the method can be found in a previous paper [8]. In the present case, we obtain converged dynamics using $n_{y,max} = 4$ and $n_{x,max} = 14$.

2.2. Dynamics in the eigenstate basis

In cases where the hyperfine interaction between the two active electrons and the semiconductor nuclei surrounding the quantum dot can be neglected, the total spin is a conserved quantity. We then need only to consider the subspace of symmetric basis functions, corresponding to singlet states, choosing the $+$ sign in equation (3). We now include a time-dependent electromagnetic field $\epsilon(t)$:

$$H_{ext} = -e\epsilon(t)X, \quad (4)$$

where $-eX = -e(x_1 + x_2)$ is the dipole operator. The dynamics is governed by the time evolution of the expansion coefficients:

$$\iota\hbar\dot{c}_{ij}(t) = \sum_{i'j'} c_{i'j'}(t)\langle i'j'|H|ij\rangle. \quad (5)$$

H is the total Hamiltonian, $H = H_0 + H_{ext}$. This system of equations is integrated using an adaptive form of Adam's method [11]. In the singlet subspace using a basis of ~4000 states, the calculations are reasonably fast. A considerable speed-up may be obtained by switching to a basis consisting of eigenstates of H_0. In this case propagation times of nanosecond duration are performed in less than a minute (on a dual-core AMD Turion 64-bit processor). We find converged results using a basis of 50 eigenstates. The coefficients in equation (5) become the coefficients of the eigenstates

$$\iota\hbar\dot{d}_k(t) = \sum_l d_l(t)\langle l|H_{ext}|k\rangle + E_k d_k(t), \quad (6)$$

where now $|l\rangle$ indicates eigenstate l with corresponding energy E_l. The matrix elements of H_{ext} are calculated based on analytic expressions obtained in the harmonic oscillator basis. The required matrix elements are given in detail in Popsueva *et al* [8].

2.3. Hyperfine interactions

A particular source of decoherence in double quantum dot molecules is the hyperfine interaction with the surrounding substrate nuclei, which has a characteristic timescale of a few nanoseconds [12]. To study this interaction from first principles, spin couplings for ~10^6 nuclear spins surrounding the electrons must be included. The magnitude of the interaction is consistent with a random magnetic field of a few mT. For the timescale of the experiment (50 ns, see 2.4) the magnetic field is taken to be constant and its spatial dependence can, to a good approximation, be represented by a step function [7]:

$$\mathbf{B}_N = \begin{cases} (B_x\mathbf{e}_x + B_y\mathbf{e}_y + B_z\mathbf{e}_z), & \text{for } x \geqslant 0 \\ 0, & \text{otherwise.} \end{cases} \quad (7)$$

The hyperfine interaction term which is to be included in H_{ext} is then given by

$$H_N = \gamma_e \sum_{i=1,2} \mathbf{S}_i \cdot \mathbf{B}_N, \quad (8)$$

where $\mathbf{S}_i$ is the spin operator of electron i and $\gamma_e = g^*\frac{e}{2m_e}$ (gyromagnetic ratio) with $g^* = -0.44$ (effective g factor). In this semiclassical picture, we must consider an ensemble of quantum dot systems, each with a different
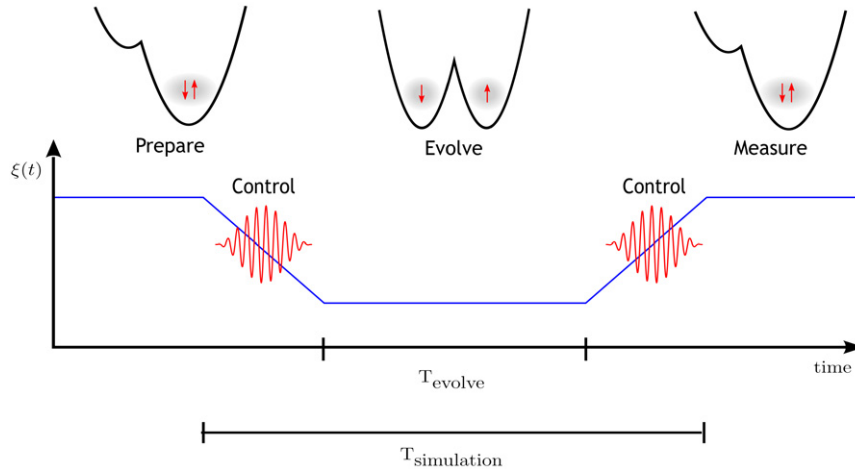
Figure 1. Illustration of a spin dephasing experiment in a double quantum dot molecule, as we model it in our simulations. The blue (dark) line shows the slowly switched electric field that guides the two electrons from a single- to a double-dot configuration. During the switch, control pulses may be applied in order to guide the electrons into excited states.

random nuclear magnetic field, and average over the ensemble to obtain physical quantities. The ensemble is created from a normal distribution of magnetic fields about zero, $P(\mathbf{B}_N) = 1/(2\pi B_{nuc}^2)^{\frac{3}{2}} \exp(-\mathbf{B}_N \cdot \mathbf{B}_N/2B_{nuc}^2)$ [13]. B_{nuc} can be determined by experiments and is of the order of 1 mT [10]. The interaction term induces couplings between the singlet and triplet states and between the different triplet states, necessitating the inclusion of both subspaces in the calculations. Details of the matrix elements involved can be found in appendix A. We remark that other types of interactions with external degrees of freedom, such as interactions with electron spins or phonons, can be introduced formally in the same way.

2.4. Dynamics in the adiabatic basis

Experimental studies of spin dephasing in quantum dots require preparation of two electrons in the singlet ground state. In a recently reported experiment by Petta *et al* [5], this is achieved by adjusting the gate voltage, creating an electric field over the double dot, and deforming the confining potential until at large field strength it becomes essentially a single dot, as illustrated in figure 1. The electrons are then allowed to tunnel into the trapping region, forming a singlet state. Reversing the gate voltage slowly guides the electrons into the ground state of a delocalized double-dot configuration. The system is allowed to evolve here for ∼50 ns during which interaction with the surrounding spin bath takes place. Readout of the singlet state population, which gives the degree of spin dephasing, is performed by once more tuning the gate voltage to a single-dot configuration.

　　To simulate the experiment, the one-center basis approach as described above is unsuitable, as a very large number of basis states is required to accurately represent the wavefunction when the electric field is large. In addition, including the triplet states adds a factor of four to the basis size, making the calculations prohibitively time-consuming. Even switching to the diabatic basis, also described above, yields lengthy

calculations. However, we observe that the energy spectrum as a function of electric field strength displays well-separated states with clear anticrossings. These considerations lead us to select instead an adiabatic basis approach, where the wavefunction is expanded in eigenstates of the instantaneous electric field:

$$\Psi(\mathbf{r}_1, \mathbf{r}_2, t) = \sum_k a_k(t)\theta_k(\mathbf{r}_1, \mathbf{r}_2; \xi) \otimes |S\rangle, \qquad (9)$$

where $|S\rangle$ refers to either a symmetric (triplet) or antisymmetric (singlet) spin function. Note that the electric field is time-dependent, $\xi = \xi(t)$, but we have dropped the explicit reference to t in order to simplify notation. The governing equations for the coefficients, derived in appendix B, are

$$\hbar\dot{\mathbf{a}}(t) = \left(-e\dot{\xi}\mathbf{K}(\xi) - \iota\varepsilon(\xi)\right)\mathbf{a}(t). \qquad (10)$$

This expression is an equivalent reformulation of the TDSE. The anti-Hermitian matrix $\mathbf{K}(\xi)$ is computed for a set of electric field values, $\{\xi_m\}$, using the numerically obtained eigenstates and eigenvalues together with analytical matrix elements of the symmetrized harmonic oscillator functions $|ij\rangle$, defined in equation (3):

$$\mathbf{K}_{kl}^m = \frac{1}{\epsilon_k^m - \epsilon_l^m} \sum_{ij} \sum_{i'j'} c_{ijk}^m c_{i'j'l}^m \langle ij|X|i'j'\rangle. \qquad (11)$$

The index m refers to the electric field points and $X = x_1 + x_2$.

　　Since the explicit time dependence in equation (10) is only found in the scalar function $\dot{\xi}(t)$, the matrix elements need only be computed once, speeding up the time integration. Only $\dot{\xi}(t)$ must be computed during integration, but this is inexpensive. As the numerically computed basis set is not continuous in ξ, we use a simple low-order polynomial interpolation between the ξ grid points where required by the integrator. For a sufficiently fine mesh of grid points the interpolation will be very accurate. We would like to stress that the adiabatic basis expansion above is in terms of the slowly varying electric field used to switch between the single-and double-dot configuration, and the switching time is a few nanoseconds.

2.5. Optimal control

Quantum control may be broadly divided into two sub-fields: the experimental closed loop approach and the computational approach (optimal control theory, OCT) for obtaining controls. The closed loop approach was originally suggested by Judson and Rabitz [14] in the context of laser control of chemical systems. Improvements of the method are suggested in [15, 16]. In this approach the target is chosen to be an experimentally measurable quantity, e.g. the mass ratio of two competing chemical products [17]. The OCT approach is based on solving iteratively the Schrödinger equation while updating certain control parameters. In the basic Krotov approach as presented here, the choice of initial and final (target) state is essential to the optimization scheme. In Palao and Kosloff [18], a generalization is presented to optimize unitary transformations that are independent of the initial state.

Most algorithms aim to maximize performance functionals with no requirement on the structure of the controls apart from minimizing the energy. Therefore the controls obtained are generally too oscillatory for existing laser apparatus to produce [19]. This has, so far, prevented the computational approach from being used to design real pulses for laboratory laser experiments. There have been several attempts in theory to restrict the domain of allowed controls, noteworthy Hornung *et al* [20], Von Winckel and Borzí [21] and Borzí *et al* [22]. In a manner similar to the approach presented here, Werschnik and Gross [23] introduce filtering of the Fourier components by manually projecting out unwanted frequency components. While the controls produced by OCT are becoming less complex, experimentalists develop increasingly more advanced pulse shapers capable of producing pulses with a wide range of frequency components. Recently Silberberg demonstrated control of the polarization and shape of a laser pulse on the scale of femtoseconds [24].

We now describe the iterative Krotov method [25] for optimizing optical transitions in quantum systems [26]. In the following we will describe and discuss modifications to this scheme. In general the method aims to maximize the expectation value of a positive semi-definite operator by means of an external field while minimizing the field energy. The time evolution of the system in which we want to optimize transitions is described by the time-dependent Schrödinger equation:

$$\iota\hbar\frac{\partial}{\partial t}\Psi(\mathbf{r}_1,\mathbf{r}_2,t)=[H_0-e\epsilon(t)X]\,\Psi(\mathbf{r}_1,\mathbf{r}_2,t), \qquad (12)$$

where $\epsilon(t)$ is an electric field and $X = x_1 + x_2$ as before. We have chosen to use $\epsilon(t)$ for the electric field whenever we refer to (optimized) pulses. H_0 is the field-free Hamiltonian in equation (2). Our goal is to apply control theory to find optimal pulses for population transfer from an initial state $\Phi_i = \Psi(t = 0)$ to a target state Φ_t. The states are preselected and the pulse duration is fixed to $t = T$. The optimization is done by maximizing the expectation value of a projection operator, $|\Phi_t\rangle\langle\Phi_t|$, that is, maximizing the functional $J_1[\Psi] = \langle\Psi(T)|\Phi_t\rangle\langle\Phi_t|\Psi(T)\rangle = |\langle\Phi_t|\Psi(T)\rangle|^2$. The requirement that

the field intensity should be as small as possible is achieved by minimizing a second functional, $J_2[\epsilon] = \int_0^T \mathrm{d}t\,\lambda(t)[\epsilon^2(t)]$, where the predefined function $\lambda(t)$ acts as a penalty factor, which can be used to impose an envelope on the electric field. We will use $\lambda(t) = \lambda$ unless otherwise stated. In each iteration, the updated control field is found as a solution to

$$\nabla J_a[\epsilon]=0, \qquad J_a=J_1-J_2. \qquad (13)$$

We proceed to sketch a simple implementation of the Krotov iteration algorithm. The time interval, $[0, T]$, is divided into fixed-length intervals t_i on which $\epsilon(t)$ is taken to be constant, $\epsilon(t_i) = \epsilon_{t_i}$, $t_i \in [0, T]$. The first step is to integrate the initial value problem of equation (12). For the first iteration, $I = 0$, we use some initial guess for the control, $\epsilon^0(t_i)$. The choice of initial control is by no means immaterial, as we will see later. After propagating forward, calculate the yield, $|\langle\Phi_t|\Psi^I(T)\rangle|^2$, where $\Psi^I(T)$ is the final state. If the desired yield has been reached, the iterations are terminated. If not, solve the terminal value problem:

$$\dot{\chi}=-\frac{\iota}{\hbar}\,[H_0-e\epsilon(t)X]\,\chi, \qquad \text{with}$$
$$\chi(T)=|\Phi_t\rangle\langle\Phi_t|\Psi^I(T)\rangle, \qquad (14)$$

and obtain $\chi^I(t)$. The updated control components $\epsilon_{t_i}^{I+1}$ are obtained while integrating the TDSE, equation (12), again (step-wise) with $\Psi^{I+1}(0) = \Phi_i$: for the first time interval choose $\epsilon_{t_0}^{I+1} = -\mathrm{Im}\langle\chi^I(0)|eX|\Psi^{I+1}(0)\rangle/\lambda$, and with this $\epsilon_{t_0}^{I+1}$ integrate to find $\Psi^{I+1}(t_1)$. Repeat the process for the next time interval with

$$\epsilon_{t_i}^{I+1}=-\frac{\mathrm{Im}\langle\chi^I(t_i)|eX|\Psi^{I+1}(t_i)\rangle}{\lambda}. \qquad (15)$$

The entire procedure is repeated until the maximum number of iterations or the desired yield is reached. Using the eigenstates of H_0 as basis makes it possible to perform several hundred iterations in a few hours.

The expression for ϵ_{t_i}, equation (15), is a zeroth-order approximation to the update equation given to full order in Degani *et al* [4] Although the simple iteration method described above is not guaranteed to converge monotonically, it works quite well for the system at hand. In fact this feature might even be desirable, as it acts as a 'shake-up' of the numerical calculations: the iteration scheme finds only local maxima and thus adding small perturbations to the solution through having a non-monotonic convergence might lead to even better optimal controls. Indeed, this effect was observed when performing an additional update of the control during the backward integration, cf equations (14). In this case the convergence is smoother but often stagnates around a lower maximum yield. However, we would like to point out that the technique of using backward updates has proven to be quite effective in simpler systems, acquiring extremely high yields [27, 4]. Tests using a basis of only a few states confirmed this also in our system.

The method as presented above has another restriction in that it does not discriminate between possible controls,
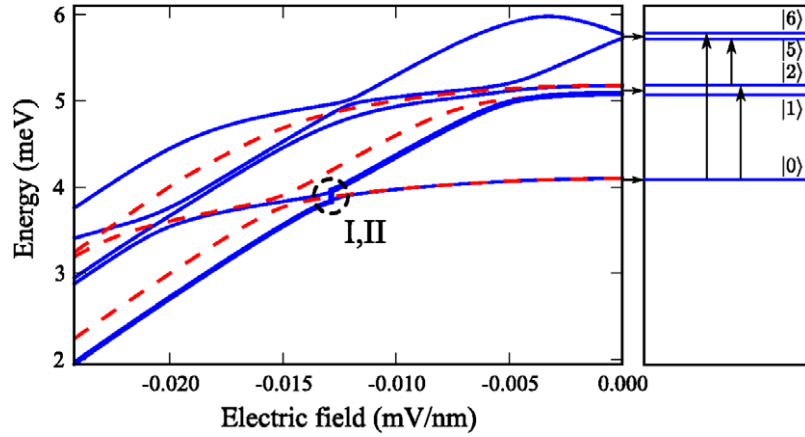
Figure 2. The two-electron double-dot spectrum as a function of electric field strength (left) and details of the spectrum at zero electric field (right). Solid lines (blue) are singlet states, dashed lines (red) are triplet states. The arrows indicate transitions referred to in the text. Only states of even *y* parity are shown.

except favoring those of low intensity. This often leads to quite complicated controls that are difficult to produce in an experimental set-up. As mentioned in Werschnik and Gross [23], a desired structure can be enforced by projecting the control onto a preferred subspace in every iteration. Instead of this brute force strategy, a modified functional, J_b, can be introduced [4] which favors low energy controls with a desired structure. This is achieved by selecting a set of 'good' controls spanning the desired subspace of the full control space. The 'bad' control subspace is then defined to be the orthogonal complement of the 'good' subspace. The weighted terms of the projection of the control onto the 'good' and 'bad' subspaces are added to the functional J_a. The new functional to maximize is

$$J_b[\epsilon] = \langle \Psi(T)|\Phi_t\rangle\langle\Phi_t|\Psi(T)\rangle$$
$$- \mathrm{d}t\, u^T(\lambda I + \lambda_1 \Phi_{\mathrm{good}} + \lambda_2 \Phi_{\mathrm{bad}})u, \qquad (16)$$

where the λ term is J_2 and $\Phi_{\mathrm{good/bad}}$ are projection operators onto the 'good' and 'bad' control subspaces, respectively. Here we have used a set of frequencies corresponding to transitions between the 10 lowest bound states as our space of 'good' controls. More specifically the space of 'good' controls is defined as the span[4] of f_{ij}, $i = 0, \ldots, 9$, $j < i$:

$$f_{ij}(t_k) = \sin^2(\pi t_k/T)\cos((E_i - E_j)t_k), \qquad t \in [t_k, t_{k+1}] \qquad (17)$$

where the $\sin^2$ envelope is chosen to encourage a gradual pulse turn-on and turn-off. Optimizing J_b instead of J_a guides the control algorithm in the direction of controls with desired frequencies. This resembles the experimental set-up in which a pulse shaper algorithm constructs a pulse using available frequencies. We would also like to stress that imposing constraints on the structure of the pulse does not necessarily compromise the yield of the transition. On the contrary, we

obtain improved yields in several cases when applying the structure functional, see also [4].

3. Results

We here present results of calculations based on the control schemes outlined in section 2, with respect to optimizing simple and combined state to state transitions in the double-dot system. This section is structured as follows. First we review the electronic spectrum and a classification of the electronic states following a diagonalization of the Hamiltonian. In section 3.2 we consider spin conserving electromagnetically driven transitions in the singlet subspace. Section 3.3 focuses on transitions during electric gate switching, indicated in figure 2 at the point of anticrossing (dashed black circle). In the latter case, H_N from equation (8) is included in H_{ext} which allows for singlet–triplet state transitions.

3.1. Electronic spectrum and state characterization

The eigenvalue spectrum in figure 2 is shown as a function of electric field strength (left). As an initial strong negative electric field is decreased, the state energies are seen to increase linearly and a number of anticrossing regions appear between states with the same symmetry. The physics of the anticrossings normally involves strong state mixing. For example, the ground state in the circled area changes from a state containing essentially both electrons in one dot to a covalent two-center state as the anticrossing is traversed. The molecular states at zero electric field (right panel) were classified and labeled in Popsueva *et al* [8].

In the present calculations we employ electric fields linearly polarized in the *x* direction. This couples states which have different *x* parity and equal *y* parity. Figure 2 shows only states with the same *y* parity as the ground state. The ground state |0⟩ is at asymptotically large dot separation identical to a linear combination of two harmonic oscillator ground states with one electron in each dot, $\phi_{n_x,n_y}(x, y)$. The two linear

---

[4] As explained in Degani *et al* [4] the values of the f_{ij} are written as columns of a matrix F. Then the columns of the matrix orth(F) form an orthonormal basis for the subspace of good controls (orth is a MATLAB and SciPy command). Thus $\Phi_{\mathrm{good}} = \mathrm{orth}(F)\,\mathrm{orth}(F)^T$ and $\Phi_{\mathrm{bad}} = I - \Phi_{\mathrm{good}}$. In the present paper SciPy (www.scipy.org) was used, where the orth command is based on the singular value decomposition.

combinations define the spatial part of the singlet (+) and triplet state (−):

$$\phi_{0,0}(x_1 - d/2, y_1)\phi_{0,0}(x_2 + d/2, y_1) \pm \phi_{0,0}(x_1 + d/2, y_1)$$
$$\times \phi_{0,0}(x_2 - d/2, y_2). \qquad (18)$$

The states $|1\rangle$, $|2\rangle$ correspond to a single exciton, i.e. a properly symmetrized linear combination where the n_x quantum numbers are raised by one in the wavefunction above. The next set of states $|5\rangle$, $|6\rangle$ are ionic states which, as the dot separation tends to infinity, become degenerate and consist of two-electron single-dot ground states with both electrons in the same dot. These two states are thus spin singlets with positive ($|5\rangle$) or negative ($|6\rangle$) reflection parity through the y axis. The spectrum of states above $|6\rangle$ is more complex until the energy levels are far above the value of the potential at $x = 0$. Then the two-electron states of a single two-dimensional harmonic oscillator are reproduced.

3.2. Spin-conserving dynamics in the singlet subspace

We first neglect spin interactions and restrict our attention to dynamics in the subspace of singlet states driven by time-dependent optical (THz) electromagnetic fields. From the ground state, transitions to the states $|2\rangle$ and $|6\rangle$ are dipole-allowed, while the state $|5\rangle$ can be reached via $|2\rangle$. We will study each of these transitions, finding that optimization procedures can produce very short pulses which achieve almost unit probability transfer.

3.2.1. Single state transitions. For the $|0\rangle$–$|2\rangle$ transition, we find that an 'intuitive' sine-squared envelope pulse tuned to the resonance frequency will transfer 98.7% of the population in 237 ps. The population of $|2\rangle$ during the pulse is shown in figure 3, labeled I (black curve). In a first attempt at optimizing this transition [3], we found that 96.5% transfer could be achieved in 111 ps, using an energy penalty functional and amplitude cutoff (II—gray curve). With the present approach, the same functional (J_a) provides better results, transferring 98.6% of the population in only 67 ps (III—red curve). Replacing the energy functional J_a with the structure functional J_b gives a slightly better final population of 99.3% (IV—blue curve).

With transition time decreased to 67 ps, the population transfer proceeds in an irregular manner for the energy penalty optimized pulse, III. This is due to the population of intermediate excited states which can be used specifically or suppressed in the advanced optimization scheme: during the pulse we find that as much at 70% of the population is transferred to highly excited states (>10). Direct transitions to these states from the ground state may be discouraged by using the structure penalty. Switching to the functional J_b, the resulting pulse causes population of higher excited states to reduce to 20% (IV). The high numbers are mainly due to the 13th excited state, which has a strong coupling to the second excited state. The resonance frequency of this transition is close to that of the $|0\rangle$–$|2\rangle$ transition, which is included in the space of good controls. Disregarding the population of $|13\rangle$, the population of the remaining higher excited states is 31%
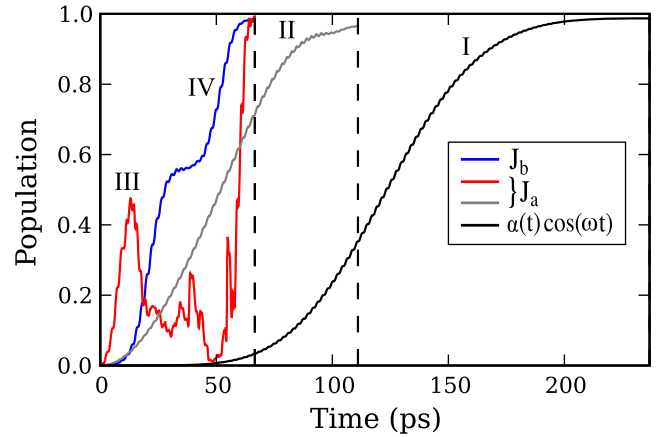

Figure 3. Population of the excited state $|2\rangle$ (starting from $|0\rangle$) as a function of time for four different pulses. Black line (I): 'intuitive pulse', $\alpha(t)\cos(\omega t)$, where $\omega = (E_2 - E_0)/\hbar = 1.5$ THz and $\alpha(t)$ is a $\sin^2$ envelope. Gray line (II): optimized pulse using the functional J_a, duration is 111 ps. Red line (III): optimized pulse using the functional J_a, duration is 67 ps. Blue line (IV): optimized pulse using the functional J_b, duration is 67 ps. The optimization was done using $\Delta t = 0.28$ ps.

and 2.7% for the J_a and J_b optimizations, respectively. The plateau structure in the population of $|2\rangle$ during the two short pulses (III and IV) is due to the transient population of $|13\rangle$.

3.2.2. Charge localization. Previously we demonstrated how charge localization in one dot can be achieved in less than a nanosecond by applying weak, resonant pulses on the system [3]. The charge localized state (CLS) is a combination of the states $|5\rangle$ and $|6\rangle$ in the third energy band of the spectrum exhibiting ionic structure, in analogy to ionic states in diatomic molecules. At large interdot separation the two states resemble the asymptotic states:

$$|g(r_{1L}, r_{2L})\rangle \pm |g(r_{1R}, r_{2R})\rangle \qquad (19)$$

where $|g\rangle$ refers to the shifted ground state of a single two-electron dot. Creating an equally weighted linear combination of these states will cause the two electrons to oscillate between localization in the left and the right dot with a period of 180 ps, inducing an AC current over the dot. This is illustrated in figure 4, where the upper panel shows the expectation value of $X = x_1 + x_2$ as a function of time, its value oscillating between the two minima of the double-dot potential. Also shown is the integrated one-electron density of the CLS at certain times during field-free time evolution, $\rho(x) = \int dy_1 \, d^2r_2 \, |\Psi(\mathbf{r}_1, \mathbf{r}_2)|^2$. In the intuitive scheme the transition to the CLS is achieved via an intermediate transition to the second excited state in the second energy band (labeled $|2\rangle$ in figure 2). This is necessary because the lowest ionic state has positive x parity and cannot be reached from the ground state directly, due to selection rules. The three transitions involved are indicated by arrows in the rightmost part of figure 2.

Figure 5 (second panel from top) shows the eigenstate population as a function of time during the sequence of resonance pulses and during the optimized pulse (bottom
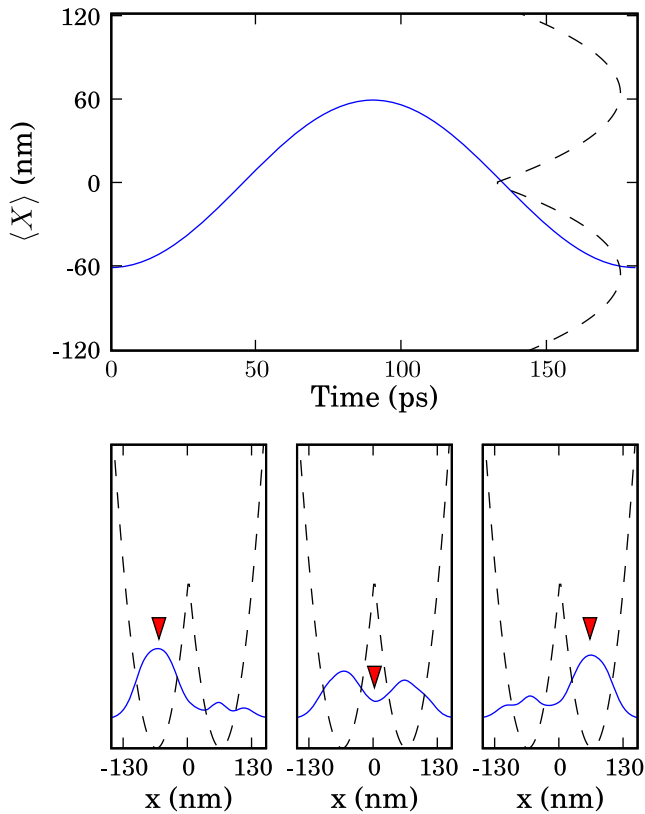
Figure 4. Field-free time evolution of the charge localized state. Upper panel: time evolution of the expectation value of $X = x_1 + x_2$. Lower panel: single-electron density averaged over the y coordinate at three different times during the time evolution: $t = 0$ ps (left), $t = 45$ ps (center) and $t = 90$ ps (right). The red markers indicate the value of $\langle X \rangle$ at the three times. The confinement potential is indicated by the dashed lines.

panel). The respective pulses are shown above. The first two pulses in the uppermost panel use a $\sin^2$ envelope whereas the last pulse uses a $\sin^2$ ramp-on over 10 oscillations.

The optimized pulse was obtained using the functional J_a with final time $T = 117$ ps and a maximum of 300 iterations. We used $\lambda(t) = 1/\sin^2(\pi t/T)$ to ensure that the pulse is zero at $t = 0$ and T (note that λ is a penalty factor, making the penalty for a non-zero field at the endpoints infinite). As seen from the population during the optimized pulse, the strategy of using the second excited state as an intermediate transition is also automatically taken advantage of by the optimized pulse. However, the detailed dynamics is much more involved. The total transition time has been brought down from 852 to 117 ps using the optimized pulse and the population of the target state has been improved from 97.2% to 99.8%. An important feature to note is that, by using a defined target state, we are also able to selectively choose the configuration of the charge localized state which is determined by the relative phase between the ionic states. We have used a target state defining the two electrons in the left dot at the end of the pulse. The charge oscillations of the CLS has a period of $\sim$180 ps, and so the relative phase evolution of the ionic states is important during the propagation. In this sense the optimal control scheme is stricter compared to the intuitive approach, where we did
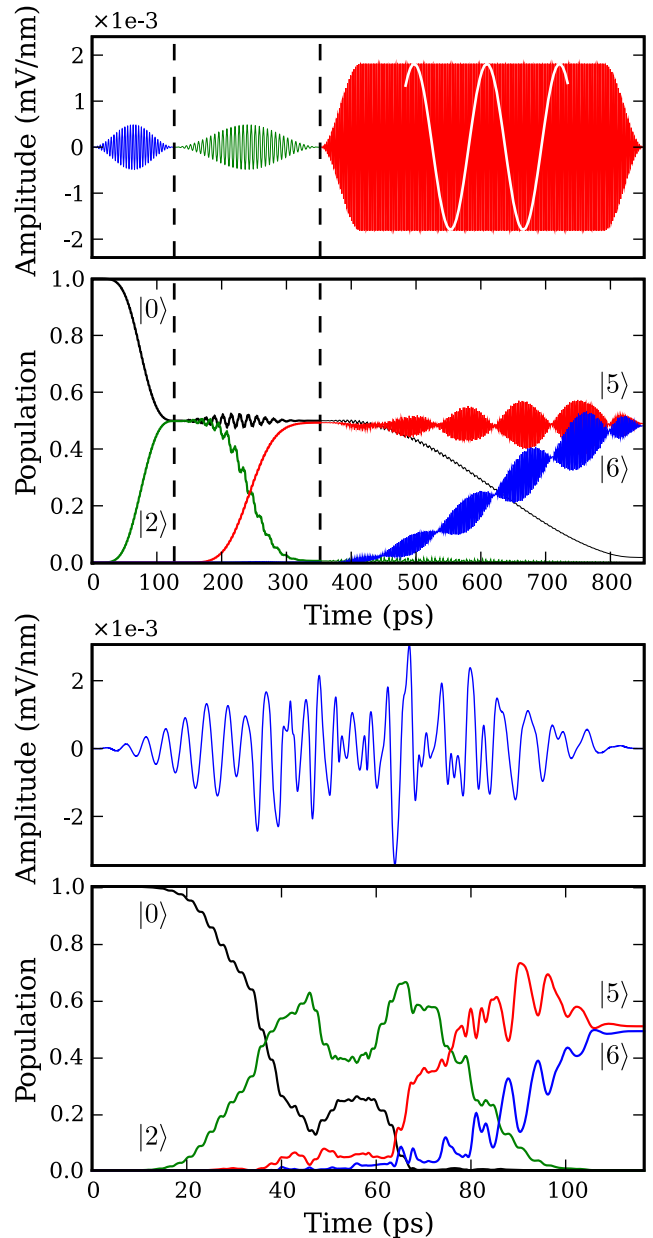

Figure 5. Driving pulse shapes and strengths (upper and third panel) and state probabilities (second and lower panel) for the transitions to a charge localized state during two different approaches. The two upper panels describe a sequence of intuitive pulses [3] and the two lower panels show optimized results based on the J_a functional (equation (13)). Transient populations are plotted for the ground state (black $|0\rangle$ curves), the second excited state (green $|2\rangle$ curves) and the two ionic states (red $|5\rangle$ and blue $|6\rangle$ curves). The white line in the upper panel is a close-up of the last pulse. The final times are 852 and 117 ps. The optimization was done using $\Delta t = 0.028$ ps.

not control the final configuration of the electrons, only the population probability of each eigenstate.

In figure 6 we have applied J_b to optimize the transition to the charge localized state. The results for $T = 67$ ps are compared with optimization using the J_a functional. Results for J_b and J_a are shown by the blue and red curves (dashed and solid), respectively (all panels). The upper panel shows the convergence of the yield (projection of the final state
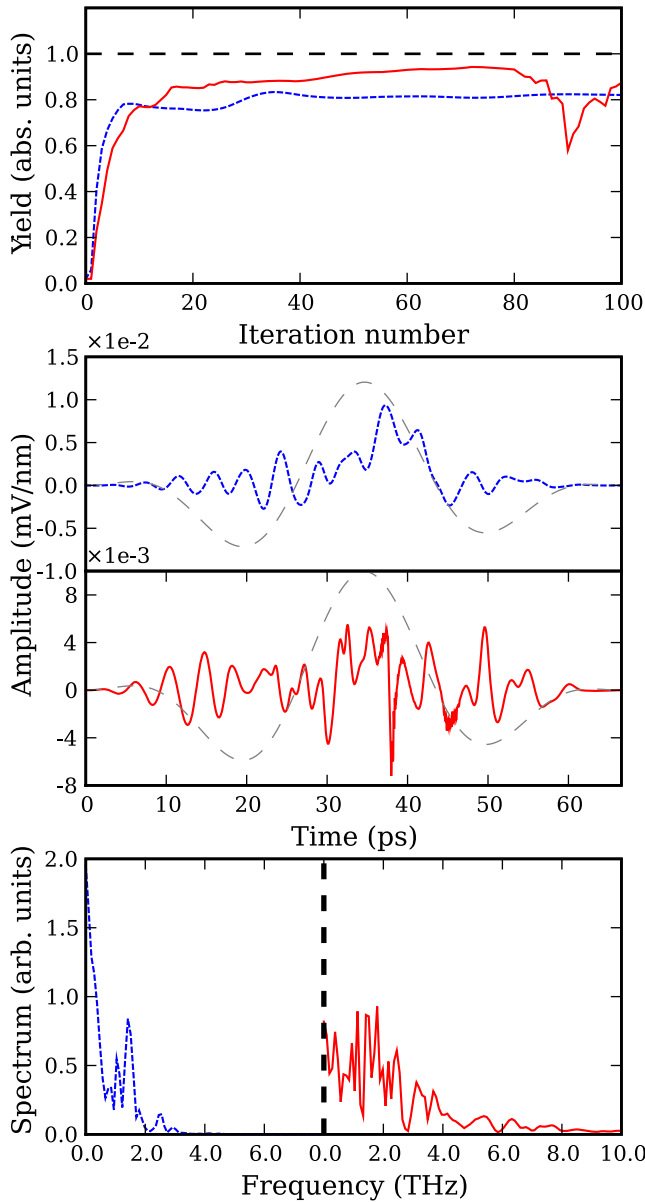
Figure 6. Properties of the optimization routines using only energy penalty (solid red curve) and including structure penalty (dashed blue curve) in the transition to the CLS. The upper panel shows the convergence of the yield as a function of iteration number. The middle panel shows the optimal pulses obtained in the two optimizations. The dashed gray curve in the background shows the initial starting field, $0.01 \sin^2(\pi t / T) \cos(0.01t)$. The bottom panel shows the frequency spectrum of the two pulses. The final time is 67 ps and the timestep used is 0.28 ps.

onto the target state) as a function of iteration. Additional iterations did not produce higher yields. The solid red curve (upper panel) is fluctuating strongly and the final pulse is also somewhat irregular. In this case we applied a low pass filter to the final pulse to get rid of very high frequency components, caused by numerical noise. We checked that removal of these components did not affect the final yield and dynamics. In general, we experience greater difficulties in achieving converging results using only the energy penalty, and the yield often converged to zero. The maximum yields for the two
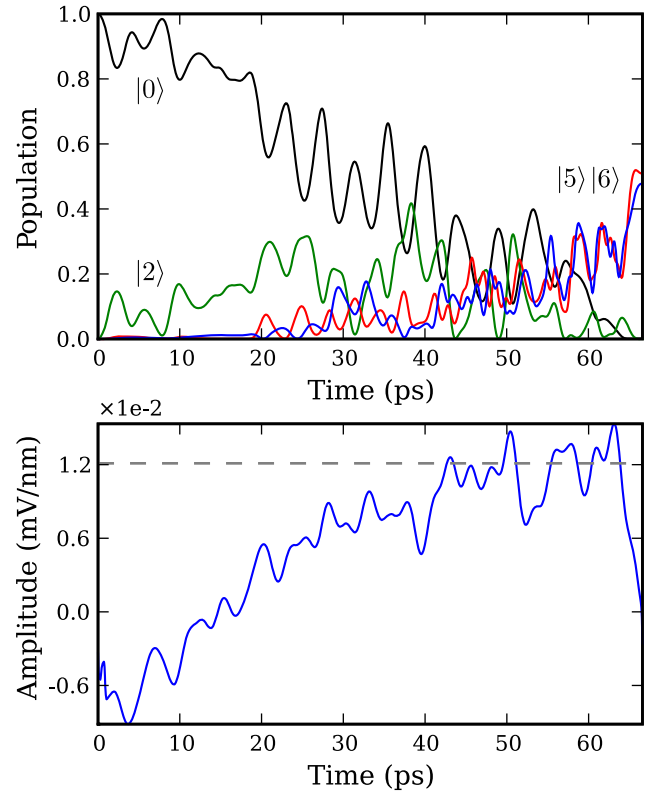

Figure 7. Pulses and probability for populating the $|CLS\rangle$ state as a function of time with a constant initial field (lower panel). Population as a function of time is plotted in the upper panel for the ground state (black $|0\rangle$ curve), the second excited state (green $|2\rangle$ curve) and the two ionic states (red $|5\rangle$ and blue $|6\rangle$ curves).

methods were 94.3% (J_a) and 83.3% (J_b). While the structure penalty strongly limits the presence of unwanted frequencies in the optimized pulse, population of excited states beyond the 10 lowest still occurs. This is again related to the existence of resonant transitions to higher excited states matching the frequency of the desired transitions. The population of excited states (>13) is for both methods $\sim$20%.

We have noticed in all our calculations that the pulse produced by the optimal control algorithm is sensitive to the choice of initial field. An example of this is shown in figure 7. Here, we start the iterations using a constant initial field (gray, horizontal curve) and consequently obtain a rather different optimal pulse compared with the one in figure 6 (dashed blue curve, middle panel), where a $\sin^2$ enveloped pulse was used (gray curve). In this case we see that the optimized pulse has retained much of its initial DC component. The maximum population of the target state is 98.6% after 419 iterations. In this case the population of highly excited states during the pulse is considerably less, with $<$10% in the 24 highest states. Optimization using only the energy penalty in this case gave a very short, high frequency and high intensity pulse, with a resulting yield of only $\sim$60%. These examples illustrate the limitations of using only energy penalty when the propagation time becomes short, and how adding structure penalty can consistently guide the control towards a wanted frequency space.

We end this section with some comments on the issue of using *y*-polarized fields. The transition to the lowest ionic state (with positive *x* parity) could in principle have been achieved using a *y*-polarized field and the third excited state in the energy spectrum, which has positive *x* parity and negative *y* parity. Note that the transition to the upper ionic state (with negative *x* parity) can only be reached via *x*-polarized fields. Using this scheme one could perform the two operations simultaneously with weak fields.

There are, however, properties of the spectrum obstructing the use of *y* polarization in this system. In the case of the CLS, the coupling between the third excited state and the lowest ionic state is virtually zero. Moreover, from the lower energy bands, there exist a multitude of strong couplings to states further up in the spectrum, precluding selective transitions to lower lying states. Numerical calculations confirm that selective state population is impractical using *y*-polarized fields.

This feature of the double-dot spectrum is related to the symmetry of the potential, particularly in the *y* direction. As noted in an earlier work [3], and as we will also see manifested later on, optical manipulation in this two-electron molecule system is actually restricted by the degree of symmetry in the potential, and control would be more easily achieved in slightly asymmetric dots. Similarly, we expect that *y*-polarized fields could be more useful in anharmonic systems.

3.3. Optimized transitions and spin interactions

In a previous paper [7], we studied the effects of spin dephasing in the quantum dot system, modeling the experiment described in section 2.4 and replicating experimental conditions as accurately as possible. We observed that, when using ultrafast electric switching (1 ps) through the anticrossing (black dashed circle in figure 2), large population transfer from the ground state to the second energy band resulted. The decoherence is largely suppressed for those states, and when the system was switched back to the single-dot configuration, 95% of the initial singlet population was regained. The suppression is explained by the fact that, at zero electric field, the singlet–triplet energy splitting is approximately 100 times greater for the second excited singlet state compared with the ground state. The 5% loss was caused by some of the population vanishing to higher excited states during passage through the anticrossings.

By applying optimal control schemes in combination with the adiabatic electric switch, the transition to excited states may be achieved with near 100% probability. An optimized pulse applied at the point of anticrossing will force a non-adiabatic transition and by targeting the desired excited state explicitly we minimize loss to other states. Figure 8 shows such a transition between the two lowest eigenstates using an optimized pulse. The optimized pulse was obtained using the structure functional J_b together with $\lambda(t) = 1/\sin(\pi t/T)$, and has a duration of $T = 67$ ps. In this case the population of other states during the pulse is completely negligible and the final population of the second excited state is as high as 99.9%. After the pulse, the system is adiabatically switched
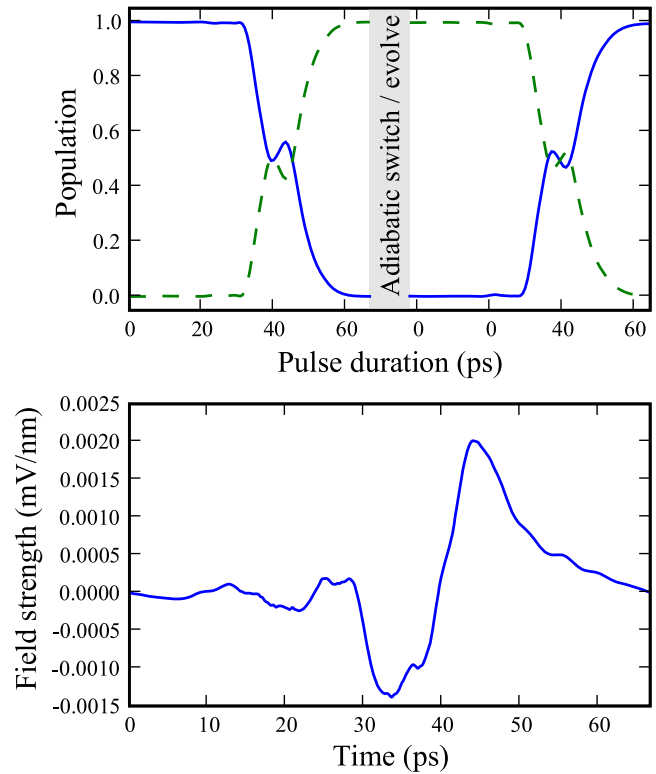

Figure 8. The optimized pulse shape (lower panel) and transient population (upper panel) of the two states involved in the circled anticrossing of figure 1. The gray area indicates a long period (50 ns) of adiabatic development of the states, before the dynamics is reversed and brought back to the ground state with the same pulse, see the text for details.

to the delocalized double-dot configuration, where the system is left to interact with the spin bath for 50 ns. Reversing the adiabatic switch and optimized pulse procedure, we find that 99.3% of the ground state population is regained. This is in sharp contrast to the original ∼50% loss of coherence found in [5]. Using OCT to suppress decoherence is here done implicitly by targeting preselected states that experience less hyperfine interaction. The Krotov method may also be used explicitly to fight decoherence, as suggested by Mohseni and Rezakhani [28].

4. Summary and conclusion

In this work we have demonstrated to what extent quantum control strategies can be applied to obtain the required transitions between electronic states of two-electron quantum dot molecules. Such transitions are non-trivial partly due to the strong electron–electron interaction, but also the large number of coupled states induced by the external fields. Nevertheless, the calculations have shown that single states and superposition of states may be reached with close to 100% probability. It has been shown that weak pulsed electric fields in the THz regime can induce transitions from the ground state to a preselected excited state within 100 ps. When applying advanced control strategies, a speed-up of more than seven times the transition time using straightforward intuitive pulses

is gained. Such control strategies also have the advantage of returning a final pulse consisting of experimentally relevant frequencies.

In the case of interactions with slowly varying external fields, which have been applied in experiments, we have shown that complete transitions at anticrossings can be obtained. This is a realistic implementation of a fully diabatic time development, which in the Landau–Zener model requires infinitely fast transitions. We also showed that the hyperfine interaction in the excited states is unimportant at the considered time scales as opposed to in the ground state. This leads us to conclude that advanced engineering of tailored pulses as here described appear as a possible route to accessing and manipulating electronic states in experiments [29, 30].

Appendix A. Matrix elements for the hyperfine interaction

In this appendix we give details of the matrix elements for the hyperfine interaction in equation (8) using the symmetrized basis of Hermite functions. The spin states are as usual

$$
\text{Triplet} \begin{cases} \chi^{\uparrow}(1)\chi^{\uparrow}(2) = |T_+\rangle \\ \chi^{\downarrow}(1)\chi^{\downarrow}(2) = |T_-\rangle \\ \frac{1}{\sqrt{2}}\left(\chi^{\uparrow}(1)\chi^{\downarrow}(2) + \chi^{\downarrow}(1)\chi^{\uparrow}(2)\right) = |T_0\rangle \end{cases} \quad \text{(A.1)}
$$

$$
\text{Singlet} \begin{cases} \frac{1}{\sqrt{2}}\left(\chi^{\uparrow}(1)\chi^{\downarrow}(2) - \chi^{\downarrow}(1)\chi^{\uparrow}(2)\right) = |S\rangle. \end{cases} \quad \text{(A.2)}
$$

The singlet has corresponding symmetric spatial functions of the form

$$
|\Psi_I(\mathbf{r}_1, \mathbf{r}_2)\rangle \Rightarrow \begin{cases} |ii\rangle = \phi_i(\mathbf{r}_1)\phi_i(\mathbf{r}_2) \\ |ij\rangle = \frac{1}{\sqrt{2}}(\phi_i(\mathbf{r}_1)\phi_j(\mathbf{r}_2) + \phi_j(\mathbf{r}_1)\phi_i(\mathbf{r}_2)). \end{cases}
$$
(A.3)

The triplet has corresponding antisymmetric spatial functions of the form

$$
|\Psi_J(\mathbf{r}_1, \mathbf{r}_2)\rangle \Rightarrow |kl\rangle = \frac{1}{\sqrt{2}}\left(\phi_k(\mathbf{r}_1)\phi_l(\mathbf{r}_2) - \phi_l(\mathbf{r}_1)\phi_k(\mathbf{r}_2)\right).
$$
(A.4)

The $\phi_i(\mathbf{r})$s are as before two-dimensional Hermite functions with $i = \{n_x, n_y\}$. Recall also the representation of the effective nuclear field, equation (7):

$$
\mathbf{B}_N = \begin{cases} \left(B_x\mathbf{e}_x + B_y\mathbf{e}_y + B_z\mathbf{e}_z\right), & \text{for } x \geqslant 0 \\ 0, & \text{otherwise.} \end{cases} \quad \text{(A.5)}
$$

Matrix elements for the $|S\rangle \longleftrightarrow |T\rangle$ *coupling*

$$
\langle \Psi_I(\mathbf{r}_1, \mathbf{r}_2); S|\hat{H}_N|\Psi_J(\mathbf{r}_1, \mathbf{r}_2); T\rangle. \quad \text{(A.6)}
$$

The first case is

$$
\langle ii; S| \sum_{i=1,2} \mathbf{S}_i \cdot \mathbf{B}_N|kl; T\rangle
$$
$$
= \frac{1}{\sqrt{2}} \sum_{x_i=x,y,z} \{\delta_{il}\langle i|B_{x_i}|k\rangle - \delta_{ik}\langle i|B_{x_i}|l\rangle\} \quad \text{(A.7)}
$$
$$
\times \langle S|S_{1x_i} - S_{2x_i}|T\rangle, \quad \text{(A.8)}
$$

and the second possibility is

$$
\langle ij; S| \sum_{i=1,2} \mathbf{S}_i \cdot \mathbf{B}_N|kl; T\rangle = \frac{1}{2} \sum_{x_i=x,y,z} \{\delta_{jl}\langle i|B_{x_i}|k\rangle
$$
$$
+ \delta_{il}\langle j|B_{x_i}|k\rangle - \delta_{ik}\langle j|B_{x_i}|l\rangle - \delta_{jk}\langle i|B_{x_i}|l\rangle\} \quad \text{(A.9)}
$$
$$
\times \langle S|S_{1x_i} - S_{2x_i}|T\rangle. \quad \text{(A.10)}
$$

Matrix elements for the $|T\rangle \longleftrightarrow |T\rangle$ *coupling.* The only possibility is

$$
\langle \Psi_I(\mathbf{r}_1, \mathbf{r}_2); T|\hat{H}_N|\Psi_J(\mathbf{r}_1, \mathbf{r}_2); T\rangle
$$
$$
\langle ij; T| \sum_{i=1,2} \mathbf{S}_i \cdot \mathbf{B}_N|kl; T\rangle
$$
$$
= \frac{1}{2} \sum_{x_i=x,y,z} \{\delta_{jl}\langle i|B_{x_i}|k\rangle - \delta_{il}\langle j|B_{x_i}|k\rangle
$$
$$
+ \delta_{ik}\langle j|B_{x_i}|l\rangle - \delta_{jk}\langle i|B_{x_i}|l\rangle\} \quad \text{(A.11)}
$$
$$
\times \langle T|S_{1x_i} + S_{2x_i}|T\rangle. \quad \text{(A.12)}
$$

The spin-coupling elements $\langle S|S_{1x_i} - S_{2x_i}|T\rangle$ and $\langle T|S_{1x_i} + S_{2x_i}|T\rangle$ for $x_i \in \{x, y, z\}$ are calculated straightforwardly using the properties of the spin operators. Their values are listed below for the different cases numbered from a to j. The spatial matrix elements, equations (A.7)–(A.9) and (A.11), are composed of simple, separable integrals over the Hermite basis functions. Since $B = 0$ over the left dot the integration in the x direction runs over half the interval:

$$
\int_0^\infty dx \int_{-\infty}^\infty dy \, H_{n_x}(x)H_{n_y}(y)H_{m_x}(x)H_{m_y}(y) \, e^{-(x^2+y^2)}.
$$
(A.13)

As the Hermite functions have well-defined parity we can use the values of tabulated integrals over the whole interval. Note that the expression above has been stripped of all factors and constants for readability. Denoting the matrices made up by the spatial integrals above, by **S**, **S − T** and **T** respectively, we can set up the following matrix:

	$|S\rangle$	$|T_0\rangle$	$|T_-\rangle$	$|T_+\rangle$
$|S\rangle$	a	b	c	d
$|T_0\rangle$	b^*	e	f	g
$|T_-\rangle$	c^*	f^*	h	i
$|T_+\rangle$	d^*	g^*	i^*	j

$$
a = 0 \qquad f = \frac{1}{\sqrt{2}}\left(B_x + iB_y\right)
$$
$$
b = B_z \qquad g = \frac{1}{\sqrt{2}}\left(B_x - iB_y\right)
$$
$$
c = \frac{1}{\sqrt{2}}\left(B_x - iB_y\right) \qquad h = -B_z
$$
$$
d = -\frac{1}{\sqrt{2}}\left(B_x + iB_y\right) \qquad i = 0
$$
$$
e = 0 \qquad j = B_z.
$$

In the Hermite basis each square in the matrix represents a $\sim$4000 × 4000 matrix. Again we convert to the adiabatic

eigenfunction basis at each electric field strength in order to keep the total size of the matrix small ($4n \times 4n$, $n = 50$).

Appendix B. Derivation of the adiabatic equations

The adiabatic basis states θ_k, depending parametrically on the time-dependent electric field ξ, are determined from the eigenvalue equation:

$$(H_0 - \xi X)\theta(\mathbf{r}_1, \mathbf{r}_2; \xi) = \varepsilon(\xi)\theta(\mathbf{r}_1, \mathbf{r}_2; \xi). \quad \text{(B.1)}$$

Here, and in the following, we switch to units in which $\hbar$, e, m_e and c are all unity in order to improve readability.

Inserting the expansion of the wavefunction, equation (9), into the TDSE:

$$\iota \frac{\partial}{\partial t} \Psi(\mathbf{r}_1, \mathbf{r}_2, t) = (H_0 - \xi X)\Psi(\mathbf{r}_1, \mathbf{r}_2, t), \quad \text{(B.2)}$$

and projecting onto each $\langle \theta_k |$ gives

$$\dot{a}_k(t) = -\sum_{j \neq k} a_j(t) \langle \theta_k | \frac{\partial}{\partial t} | \theta_j \rangle - \iota \varepsilon_k(\xi) a_k(t). \quad \text{(B.3)}$$

We now rewrite the coupling elements in a form more useful for numerical calculations by taking the time derivative of equation (B.1) for a given eigenstate $| \theta_j \rangle$, and projecting onto another state $\langle \theta_k |$:

$$\langle \theta_k | (H_0 - \xi X) \frac{\partial}{\partial t} | \theta_j \rangle - \langle \theta_k | \frac{\partial \xi}{\partial t} X | \theta_j \rangle$$
$$= \langle \theta_k | \frac{\partial \varepsilon(\xi)}{\partial t} | \theta_j \rangle + \varepsilon_j(\xi) \langle \theta_k | \frac{\partial}{\partial t} | \theta_j \rangle. \quad \text{(B.4)}$$

Rearranging, and noting that the first term on the right-hand side is zero, we obtain an expression for the time derivative coupling:

$$\frac{\partial \xi}{\partial t} \langle \theta_k | X | \theta_j \rangle = \left(\varepsilon_k(\xi) - \varepsilon_j(\xi) \right) \langle \theta_k | \frac{\partial}{\partial t} | \theta_j \rangle. \quad \text{(B.5)}$$

Upon insertion into equation (B.3) we arrive at

$$\dot{a}_k(t) = -\dot{\xi} \sum_{j \neq k} \frac{\langle \theta_k | X | \theta_j \rangle}{\varepsilon_k - \varepsilon_j} a_j(t) - \iota \varepsilon_k(\xi) a_k(t), \quad \text{(B.6)}$$

where the sum over j extends over sufficiently many adiabatic eigenstates to achieve converged results.

References

[1] D'Alessandro D and Dahleh M 2001 *IEEE Trans. Autom. Control* **46**
[2] Reetz-Lamour M, Amthor T, Deiglmayr J and Weidemuller M 2008 *Phys. Rev. Lett.* **100** 253001
[3] Sælen L, Nepstad R, Degani I and Hansen J P 2008 *Phys. Rev. Lett.* **100** 046805
[4] Degani I, Zanna A, Sælen L and Nepstad R 2008 submitted
[5] Petta J R, Johnson A C, Taylor J M, Laird E A, Yacoby A, Lukin M D, Marcus C M, Hanson M P and Gossard A C 2005 *Science* **309** 2180
[6] Laird E A, Petta J R, Johnson A C, Marcus C M, Yacoby A, Hanson M P and Gossard A C 2006 *Phys. Rev. Lett* **97** 056801
[7] Nepstad R, Sælen L and Hansen J P 2008 *Phys. Rev.* B **77** 125315
[8] Popsueva V, Nepstad R, Birkeland T, Førre M, Hansen J P, Lindroth E and Walterson E 2007 *Phys. Rev.* B **76** 035303
[9] Zumbühl D M, Marcus C M, Hanson M P and Gossard A C 2004 *Phys. Rev. Lett.* **93** 256801
[10] Petta J R, Johnson A C, Marcus C M, Hanson M P and Gossard A C 2004 *Phys. Rev. Lett.* **93** 186802
[11] Shampine L and Gordon M 1975 *Computer Solution of Ordinary Differential Equations: the Initial Value Problem* (San Francisco, CA: Freeman)
[12] Taylor J M, Petta J R, Johnson A C, Yacoby A, Marcus C M and Lukin M D 2007 *Phys. Rev.* B **76** 035315
[13] Coish W A and Loss D 2005 *Phys. Rev.* B **72** 125337
[14] Judson R S and Rabitz H 1992 *Phys. Rev. Lett.* **68** 1500
[15] Geremia J M, Zhu W and Rabitz H 2000 *J. Chem. Phys.* **113** 10841
[16] Turinici G, Bris C L and Rabitz H 2004 *Phys. Rev.* E **70** 016704
[17] Assion A, Baumert T, Bergt M, Brixner T, Kiefer B, Seyfried V, Strehle M and Gerber G 1998 *Science* **282** 919
[18] Palao J and Kosloff R 2003 *Phys. Rev.* A **68** 062308
[19] Rabitz H, de Vivie-Riedle R, Motzkus M and Kompa K 2000 *Science* **288** 824
[20] Hornung T, Motzkus M and de Vivie-Riedle R 2001 *J. Chem. Phys.* **115** 3105
[21] von Winckel G and Borzí A 2008 *Inverse Probl.* **24** 034007
[22] Borzí A, Salomon J and Volkwein S 2008 *J. Comput. Appl. Math.* **216** 170
[23] Werschnik J and Gross E K U 2007 *J. Phys. B: At. Mol. Opt. Phys.* **40** R175
[24] Silberberg Y 2004 *Nature* **430** 624
[25] Krotov V F 1996 *Global Methods in Optimal Control Theory* (New York: Dekker)
[26] Räsänen E, Castro A, Werschnik J, Rubio A and Gross E K U 2007 *Phys. Rev. Lett.* **98** 157404
[27] Zhu W and Rabitz H 1998 *J. Chem. Phys.* **109** 385
[28] Mohseni M and Rezakhani A T 2008 arXiv:0805.3188v2
[29] Stepanov A, Hebling J and Kuhl J 2004 *Opt. Express* **12** 4650
[30] Reimann K 2007 *Rep. Prog. Phys.* **70** 1597